

Oxidation of iron at 600 °C – experiments and simulations

H. Larsson*, T. Jonsson, R. Naraghi, Y. Gong, R. C. Reed and J. Ågren

Pure iron has been oxidized at 600 °C and 1 bar in dry O₂ (oxygen partial pressure 0.05, bal. N₂) and the mass gain as well as the thicknesses of the individual oxide phases have been measured. The oxidation process has been simulated using a modified version of the homogenization model as implemented in Dictra; this has helped to rationalize the kinetics of oxide scale formation and in particular the evolution of the hematite (Fe₂O₃), magnetite (Fe₃O₄), and wustite (FeO) which form. Independently assessed thermodynamic and kinetic Calphad databases are needed for the calculations; details of these are given. Reasonable agreement between simulation results and experimental data is obtained, though it is concluded that the large influence of grain boundary diffusion on the oxidation rate needs further consideration.

1 Introduction

It is well known that steels can suffer from oxidation, moreover that this phenomenon can limit the temperature capability of these materials. Iron-based oxides are very often the ones which are formed – for example when the Cr content is lower than about 9 wt% and even in stainless steels after so-called breakaway oxidation, when the flux of Cr to the surface scale is no longer sufficient for chromia formation. The importance of the oxidation process – in scientific, technological, and even economic terms – is emphasized in the great body of literature which exists concerning this phenomenon, see Refs. [1–8].

In an ideal world, accurate numerical models would exist for the oxidation process which are based upon the underlying thermodynamics and mass transport processes which are prevalent. But although substantial progress in this regard has been made in recent years, models of the greatest predictive power or else sensitive to the underlying alloy composition – for example suitable for failure analysis or alloy design

H. Larsson, J. Ågren

Unit of Structures, Department of Materials Science and Engineering, KTH Royal Institute of Technology, SE-10044 Stockholm (Sweden)
E-mail: hlarsson@kth.se

T. Jonsson

High Temperature Corrosion Centre, Chalmers University of Technology, SE-41296 Göteborg (Sweden)

R. Naraghi

Thermo-Calc Software, Norra Stationsgatan 93, SE-11364 Stockholm (Sweden)

Y. Gong, R. C. Reed

Department of Materials, Department of Engineering Science, University of Oxford, Parks Road, Oxford OX1 3PH (UK)

purposes – are still rare. Why is this? One reason may be the complexity of the situation, even for the binary Fe–O system, the consideration of which is a prerequisite for any treatment of multicomponent iron-base alloys. In this case, iron forms a layered oxide scale when exposed to oxygen at high temperatures. Above 573 °C, the scale consists of a hematite (Fe₂O₃) top layer, a magnetite (Fe₃O₄) middle layer, and a wustite (FeO) bottom layer. The oxidation of iron in the temperature range 580–650 °C has been investigated previously [9–11]. Generally, the oxidation kinetics is reported to obey a parabolic rate law; however, the precise rate-controlling steps need clarification, rationalization, and modeling.

There is a significant body of work which has aimed at the mathematical modeling of the oxidation process in metals and alloys. Analytical equations describing the evolution of an external oxide scale on a binary alloy were first derived by Wagner [12]. Simulations of external oxide scale growth using independently assessed data have been performed by Narita et al. [13] and Hallström et al. [14]. Calphad-type databases were used by Hallström et al. who simulated growth of Cr₂O₃ on pure Cr with the Dictra software [15] using a moving phase boundary approach. In principle, a similar approach can also be used to simulate oxidation of iron. However, the present work is intended as a first step toward simulation of oxidation of multicomponent alloys and in those cases the microstructural evolution exhibits phenomena – for example miscibility gaps and internal oxidation zones – that cannot be simulated with the approach used by Hallström et al. For this reason a different approach is used in the present paper; an approach is employed which will allow its future extension to full multicomponent analysis.

The aim of the present paper is to simulate the oxidation of iron using a modified version of the homogenization model as implemented in the computer-simulation software Dictra [16,17].

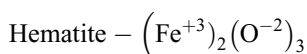
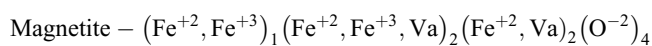
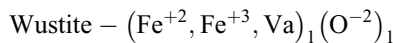
The simulation model is coupled with Calphad-type databases, so that the greatest fidelity to the underlying thermodynamics is respected. Here, the simulations are carried out with a development version of Dictra. The results from the simulations are compared with experimental results from the oxidation of pure iron performed at 600 °C. The work includes a detailed microstructural investigation of the oxide scales formed up to 24 h exposure, which is important for the purposes of model testing, calibration, and validation.

2 Thermodynamic and kinetic description

The thermodynamic and kinetics of the Fe–O system have been independently assessed by using the so-called Calphad method. This method consists of modeling the thermodynamics and kinetics of each phase using a mathematical expression and techniques to assess a number of model parameters to fit the experimental thermodynamic data, phase diagrams as well as kinetic information of a system. Here a brief summary is given.

2.1 Thermodynamic model

The iron–oxygen system has been subjected to several thermodynamic assessments [18,19]. The assessment by *Sundman* [18] is widely accepted in various thermodynamic databases and it has been the basis of the present work. In *Sundman's* assessment, the solid phases are all described using the compound energy formalism (CEF) [20] as:



where Fe^{+2} , Fe^{+3} , O^{-2} , and Va (vacancy) are constituents in each set of parentheses which represent a specific sublattice and the factors are the stoichiometric coefficients. In the assessment mentioned above, hematite is modeled as a stoichiometric phase, and deviation from the stoichiometric composition of magnetite and hematite depends upon the oxygen potential in the surroundings.

The Gibbs energy of each phase is described as:

$$G_m = \sum_{I_0} P_{I_0}(Y)^0 G_{I_0} + RT \sum_{s=1}^n \alpha_s \sum_{i=1}^{n_s} y_i^s \ln(y_i^s) + {}^{\text{phys}}G_m + {}^E G_m \quad (1)$$

where I_0 is a constituent array of zeroth order and $P_{I_0}(Y)$ is the corresponding product of the site fractions. The zeroth order constituent array has one constituent on each sublattice. The ${}^0G_{I_0}$ represents the Gibbs energy of the compound I_0 . The factor a_s is the number of sites on sublattice s and y_i^s denotes

the site-fraction of constituent i on sublattice s . ${}^{\text{phys}}G_m$ represents the contribution to the Gibbs energy due to physical properties like the magnetic transitions and ${}^E G_m$ is the excess Gibbs energy.

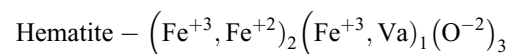
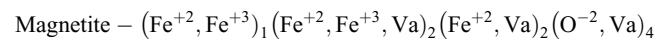
$${}^E G_m = \sum_{I_1} P_{I_1}(Y) L_{I_1} + \sum_{I_2} P_{I_2}(Y) L_{I_2} + \dots \quad (2)$$

where I_1 is a constituent array of first order and L_{I_1} is the interaction parameter defined by I_1 . The interaction parameters can be represented by a *Redlich-Kister* expansion [21].

A constituent array of first order has two constituents in one sublattice but only one in the remaining sublattices. A constituent array of second order could have either three interacting constituents on one sublattice or two interacting constituents on two different sublattices. Higher order terms may also be added.

The magnetic contribution to the Gibbs energy is given by the model proposed by Ref. [22] and adapted by Ref. [23].

To be able to use this description for modeling diffusivity of iron species, *Kjellqvist* et al. [24] have modified the hematite description with an additional interstitial sublattice with Fe^{+3} and vacancies, while introducing Fe^{+2} in the first sublattice to maintain the electroneutrality. Similarly, the sublattice descriptions were further modified by the present authors with additional vacancy in the oxygen sublattice to be able to model the diffusivity of oxygen:



The details of thermodynamic description modifications as well as the kinetic parameters described in the following section will be published elsewhere [25].

2.2 Oxide diffusion model

When CEF is applied in order to describe the thermodynamic properties of the oxides, the constituents on each sublattice are ions. The ions can diffuse through the same sublattices if vacancies are also available on the same site. Thus we can express the mobility M_i of ion i on each sublattice in a lattice (oxygen) fixed frame of reference as:

$$M_i = \frac{1}{c_i} \frac{a_s}{a_o} y_i^s (y_{\text{Va}}^s M_{i\text{Va}}^s) \frac{1}{V_m} \quad (3)$$

where c_i is the concentration of the diffusing ion per mole of anion sites ($c_i = n_i/V_m$).

M_i is related to the tracer or self-diffusion coefficient D_i^* by comparing the limiting case of zero electrical-potential gradient

to Fick's first law as:

$$M_i = \frac{D_i^*}{RT} \quad (4)$$

By substituting Equation (3) in Equation (4) and integrating over the sublattices, we derive the tracer diffusion coefficient as:

$$D_i^* = RT \sum_{s=1}^n \frac{a_s}{a_o} y_i^s y_{Va}^s M_{iVa}^s \frac{1}{n_i} \quad (5)$$

where y_i^s is the fraction of ion i on the s sublattice. a_s and a_o denote the stoichiometric coefficients of sublattice and oxygen sublattice respectively. M_{iVa} is the mobility factor which represent the thermally activated jumps and has the form:

$$M_{iVa} = M_{iVa}^0 \exp\left(\frac{-Q_{iVa}}{RT}\right) \frac{1}{RT} \Gamma^{\text{mg}} \quad (6)$$

R is the gas constant, T the temperature, M_{iVa}^0 is a frequency factor, Q_{iVa} is an activation enthalpy, and Γ^{mg} is a factor taking into account the effect of ferromagnetic transition.

If the ferromagnetic effect for the phase can be ignored, the mobility can be simplified to:

$$M_{iVa} = \exp\left(\frac{-Q_{iVa} + RT \ln M_{iVa}^0}{RT}\right) \frac{1}{RT} = \exp\left(\frac{\Delta G_{iVa}}{RT}\right) \frac{1}{RT} \quad (7)$$

In general the parameter ΔG_{iVa} can depend on composition, the temperature, and the pressure. In the spirit of the Calphad approach, the composition dependence of ΔG_{iVa} is represented as

$$\Delta G_{iVa} = \sum_{I_0} P_{I_0}(Y) \Phi_{I_0} + \sum_{I_1} P_{I_1}(Y) \Psi_{I_1} + \sum_{I_2} P_{I_2}(Y) \Psi_{I_2} + \dots \quad (8)$$

where Φ_{I_0} is the value at each endpoint of the composition space (I_0) and Ψ_{I_1} is the interaction parameter defined by I_1 .

The mass transport of the constituents on a specific sublattice will thus vary with the vacancy site fraction and the site fractions of the constituents. The site fractions depend on the overall composition of the phase, which in turn depend on the oxygen activity. The end result is that the overall, effective, mass transport in the oxide will depend sensitively on the oxygen partial pressure, see Ref. [26] for a detailed discussion on this subject.

The mobilities of iron in iron oxides were assessed by Hallström et al. [26,27]. The oxygen mobilities were recently assessed by Naraghi [25]. Iron mobilities were also re-assessed due to the changes in thermodynamic models [25]. The parameters obtained from the assessment were added to the kinetic database and used in the simulations. The impurity diffusivity of oxygen in ferrite was assessed by Takadi et al. [28]

and the tracer diffusivity of iron in ferrite was assessed by Jönsson [29].

2.3 Element mobilities

In simulations it is the effective mobilities of the elements rather than the mobilities of ions that are considered. These are evaluated in accordance with the model presented by Hallström et al. [26]. As they did not present the general expression for the diffusional mobility it will be given here (see also Ref. [27]). The mobility M_j^r of element j in phase r is given by

$$M_j^r = \frac{\sum_s a_s^r \sum_k b_{jk} y_k^{rs} z_{Va}^{rs} M_{kVa}^{rs}}{\sum_s a_s^r \sum_k b_{jk} y_k^{rs}} \quad (9)$$

where s is sublattice index and k is species index. The other parameters are defined as follows:

- M_{kVa}^{rs} is the mobility of species k on sublattice s in phase r .
- a_s^r is the number of sites on sublattice s in phase r .
- b_{jk} is the number of moles of element j per mole formula unit of species k .
- y_k^{rs} is the site fraction of species k on sublattice s in phase r .
- z_{Va}^{rs} is identical with y_{Va}^{rs} if vacancy is a defined constituent on the sublattice, otherwise it is set equal to one.

2.4 Grain boundary diffusion

In the following so-called type A kinetics [30] is assumed to take grain boundary diffusion into account

$$M_k^{\text{tot}} = f^{\text{gb}} M_k^{\text{bg}} + (1 - f^{\text{gb}}) M_k^{\text{bulk}} \quad (10)$$

$$f^{\text{gb}} = \delta/d \quad (11)$$

$$M_k^{\text{gb}} = M_{k0}^{\text{bulk}} \exp\left(\frac{-\alpha Q^{\text{bulk}}}{RT}\right) \quad (12)$$

where δ is the width of the grain boundary, d is grain size, and α is a factor taking into account the lower activation energy ($\alpha < 1$) for diffusion along grain boundaries compared to in the bulk. The value assumed for δ is often 0.5 nm and that value was also used in the present work. It is important to note that a more complex expression is used for the bulk mobilities than a single Arrhenius expression, as discussed above. Thus, an "effective" bulk activation energy must be evaluated for a given state.

For certain systems, and certain temperature ranges, it may be more appropriate to perform specific assessments of the grain boundary diffusion rather than base the evaluation on bulk mobility data, though this is made difficult due to the scarcity of experimental data.

3 Simulation model

The basis of the so-called homogenization simulation model has been described in detail previously [16,17], but for the convenience of the reader a brief description is included in the present work. In addition, the model has been slightly modified to allow for simulations of oxidation.

3.1 An outline of the simulation model

If correlation effects are ignored, the flux of an element k [$\text{mol m}^{-2} \text{s}^{-1}$] in a single phase region along spatial coordinate z in the lattice-fixed frame is usually written as (see, for example, Ref. [31])

$$J_k = -M_k c_k \frac{\partial \mu_k}{\partial z} \quad (13)$$

where M_k is the mobility, c_k the concentration, and μ_k the chemical potential of k , respectively. In Equation (13), the local vacancy concentration has been incorporated in the mobility, in accordance with Equation (9), and it is assumed that the vacancy chemical potential is zero everywhere.

In order to evaluate the temporal evolution of the concentration fields $c_k(z,t)$ of the n elements of the system, the expression for the flux is combined with the equation of continuity

$$\frac{\partial c_k}{\partial t} = \frac{\partial}{\partial z} (-J_k) \quad k = 1, \dots, n \quad (14)$$

The system of n , generally non-linear, partial differential equations represented by Equation (14) can be solved using many different kinds of numerical techniques. Specific considerations are, however, needed when the equations are solved in the lattice-fixed frame of reference as discussed in Ref. [32]. Some general comments on the implementation used in the present work is given below.

The homogenization model is intended for multiphase diffusion problems. Computationally, the problem is transformed into a single phase problem by homogenization, i.e., it is the average, or effective, thermodynamic and kinetic properties of the phases present locally that are considered. The model relies on the assumption that the material is fully equilibrated locally with respect to those phases that are entered into a simulation. This means that the local phase fractions, phase compositions, chemical potentials, etc. are obtained from an equilibrium calculation with the local overall composition as an equilibrium condition. In the present case, simulations are only performed for the binary system Fe–O under isobarothermal conditions and this means that locally only one or two phases may be stable, in accordance with the phase rule.

The transport property of individual phases that is considered is the product of mobility times solubility and it is, therefore, convenient to define

$$\Gamma_k^\phi = M_k^\phi c_k^\phi = M_k^\phi \frac{x_k^\phi}{V_m^\phi} \quad (15)$$

for each phase ϕ . An estimate of the effective transport property of the multiphase mixture Γ_k^* is then obtained by applying some combining rule, e.g., rule of mixtures, inverse rule of mixtures (the so-called *Wiener* bounds [33]) or *Hashin-Shtrikman* bounds [34]. If the rule of mixtures is used the expression for Γ_k^* becomes

$$\Gamma_k^* = \sum_{\phi} f^\phi \Gamma_k^\phi \quad (16)$$

where f^ϕ is the local volume fraction of phase ϕ .

The flux expression Equation (13) can then be written as

$$J_k = -\Gamma_k^* \frac{\partial \mu_k^{\text{l.eq.}}}{\partial z} \quad (17)$$

where the superscript l.eq. has been added to emphasize that a locally equilibrated chemical potential is assumed.

Previously [16,17], a simplified treatment of volume has been used in which it was assumed that only substitutional elements contribute to volume and that the partial molar volume of all substitutional elements is constant and equal. This simplification has been very useful in many cases, but in the case of oxidation of iron it is not convenient since in the oxides it is the oxygen that is substitutional, but in the ferrite it is the iron. Thus, the assessed molar volumes of the thermodynamic description is used in this work. Also, previously the fluxes have been transformed to a volume-fixed frame of reference which is straightforward when the simplified treatment of volume is used. When the assessed molar volumes are used it is more natural to perform the simulation in a lattice-fixed frame of reference since the local molar volume will change as a result of the diffusion process.

3.2 Implementation of the model

The model has been implemented using a finite volume approach, i.e., the domain is divided up into a number of control volumes that may have varying thicknesses, with semi-implicit (trapezoidal rule) or fully implicit (Euler backward) time-stepping. Only the average composition of the finite volumes is considered.

When evaluating the flux between sources with large changes in composition it has been found to be advantageous to use the following flux expression [35,36]

$$J_k = \frac{-M_k RT}{V_m \Delta z} \sqrt{x_k^1 x_k^2} 2 \sinh \left(\frac{\Delta \mu_k}{2RT} \right) \quad (18)$$

where x_k^1 and x_k^2 are the mole fractions of component k at plane/source 1 and 2, respectively, and Δz is the center-to-center distance between those planes/sources. In the limit $\Delta z \rightarrow 0$, where $\Delta \mu_k \ll 2RT$, Equation (18) reduces to Equation (13).

For use in the present context it is natural to rewrite Equation (18) slightly in the following form

$$J_k = \frac{-RT}{\Delta z} \sqrt{\Gamma_k^* \Gamma_k^{2*}} 2 \sinh\left(\frac{\Delta\mu_k}{2RT}\right) \quad (19)$$

The basic flux expression used in simulations is Equation (19), but see also Section 3.3.

3.3 Diffusion across interfaces

In binary systems during diffusion controlled growth, a transition from one single phase region to another will always be quite sharp, in view of the phase rule. Phase interfaces are not introduced explicitly in the present simulation model and transitions between different phase regions will simply occur in those finite volumes where, at a given moment, two phases are stable. In the iron–oxygen system it is not believed that the trans-interface diffusion should be rate limiting. However, if the bulk mobilities are used at such positions in the simulation domain that may be the, unintended, end effect. Consider for example the diffusion of the iron from the ferrite and into the wustite. The mobility of iron is much lower in the ferrite than in the wustite and the factor $(\Gamma_{\text{Fe}}^{1*} \Gamma_{\text{Fe}}^{2*})^{1/2}$ in the flux expression Equation (19) may then get an unreasonably low value at finite volumes where the transition occur. Pragmatically, a “high enough” value for the mobility of iron in ferrite may be substituted for the assessed value. This is an option in the binary case since the diffusivity value of iron in the ferrite should not affect the growth rate of the oxides and there is no interdiffusion in the ferrite to take into account. However, if the present model is applied to, say, Fe–Cr–O it is necessary to treat the diffusion in the ferrite in a correct manner, i.e., the assessed mobility values for iron and chromium in the ferrite should then be used.

Tentatively, a “degree of phase transition” between two finite volumes may be written as the following sum taken over all phases taking part in the simulation

$$\frac{1}{2} \sum_{\phi} |\Delta f^{\phi}| \quad (20)$$

where Δf^{ϕ} is the difference in the volume fraction of phase ϕ . The flux expression Equation (19) may then be adjusted to accommodate for adjusted kinetics for transfer across interfaces in the following manner

$$J_k = \frac{-RT}{\Delta z} \left[\left(\frac{1}{2} \sum_{\phi} |\Delta f^{\phi}| \right) M_k^{\text{trans}} \sqrt{c_k^1 c_k^2} + \left(1 - \frac{1}{2} \sum_{\phi} |\Delta f^{\phi}| \right) \sqrt{\Gamma_k^* \Gamma_k^{2*}} \right] 2 \sinh\left(\frac{\Delta\mu_k}{2RT}\right) \quad (21)$$

The present model is by no means intended for simulations of interface controlled reactions and M_k^{trans} may thus, ad hoc, be taken as the highest mobility value for element k among all locally present phases. This will have the intended result that the transfer across the interface will not be rate limiting (see Ref. [36] for a discussion on this topic). On the other hand, if a physically

realistic value of the trans-interface mobility (see for example Ref. [37]) would be used the rate of oxidation would generally be overestimated since the width of finite volumes is not, and should not be, comparable to the width of interfaces.

3.4 Kirkendall porosity

Semi-quantitative evaluation of the amount of Kirkendall porosity has been performed by several authors, see, e.g., Refs. [38–40]. In the present work, it is assumed that annihilation of vacancies on the anion sublattice gives rise to Kirkendall porosity. This assumption will presumably yield an upper bound on the amount of porosity since a certain amount of vacancies may annihilate before giving rise to pores. Thus, on the anion sublattice, the vacancy flux equals

$$J_{Va} = -J_O \quad (22)$$

The temporal evolution of the concentration of vacancies is given by the equation of continuity if a source term q_{Va} is included

$$\frac{\partial c_{Va}}{\partial t} = \frac{\partial}{\partial z} (-J_{Va}) + \dot{q}_{Va} \quad (23)$$

A negative value of q_{Va} corresponds to annihilation and a positive creation of vacancies. By assuming that the local amount of vacancies is essentially constant and locally equilibrated we have

$$\frac{\partial c_{Va}}{\partial t} \simeq 0 \quad (24)$$

Thus,

$$\dot{q}_{Va} = \frac{\partial J_{Va}}{\partial z} \quad (25)$$

The amount of porosity is then obtained by integrating over those areas where $q_{Va} < 0$.

4 Results

4.1 Experimental observations

Experimental results are presented in Figs. 1–5. All presented results pertain to oxidation of pure iron in dry oxygen at 600 °C.

A FIB image of the surface morphology is shown in Fig. 1. The oxide surface is rough and undulating. There were no large changes in oxide morphology with exposure time.

Figure 2 shows FIB images of ion-milled cross-sections of the oxide scales formed after 1 and 3 h exposure. SEM/EDX and SEM backscattered electron (BSE) imaging were used together with XRD to determine the phases. It was concluded that after 1 h exposure a thin hematite layer covered a thicker magnetite layer. Wustite was found at the metal oxide interface. The borders

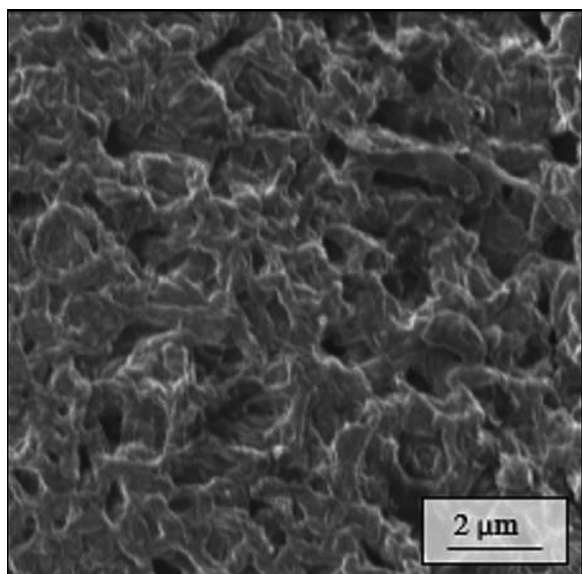


Figure 1. FIB plan view image showing the surface morphology formed after 1 h in dry O_2 at 600 °C.

between the magnetite and the wustite are indicated in the images.

The scale microstructure found after 1 h consists of an approximately 0.5 μm thick hematite layer consisting of small grains. The magnetite layer is about 8 μm thick and consists of 1–2 μm diameter grains. The variation in oxide grain size is partly an imaging effect because the cross-section shows a

two-dimensional image of the three-dimensional oxide grains. The magnetite layer also contains voids in the outer part of the scale. Below the magnetite an approximately 2.5 μm thick wustite layer with a typical grain size of 1–2 μm could be found. Voids could in addition be found at the wustite/metal interface where the wustite grains also are smaller. The scale thicknesses measured in the cross-sections are in accordance with the mass gain and thicknesses reported in Refs. [41,42]. However, there is a relatively large local variation in scale thickness after 1 h.

The wustite and magnetite layers grow between 1 and 3 h exposure time while there is no significant growth of the hematite layer. After 3 h exposure the magnetite layer is about 11–12 μm . The magnetite grains have grown with exposure time, being 2–3 μm after 3 h. The magnetite layer still contains voids in the outer part of the scale. The voids are after 3 h exposures larger. The wustite layer has grown in thickness to about 6–7 μm . A local thickness variation could be observed in the wustite layer if measured over a wider region. The grains in the wustite have also grown with exposure time. A thin region with smaller oxide grains and voids are observed at the oxide/metal interface. The thickness of this layer is similar as after 1 h.

A cross-section after 24 h is shown in Fig. 3. After this time the wustite is the individually thickest oxide. The growth rates thus exhibit non-parabolic behavior. This could at least in part be explained by grain growth that results in a decreasing relative contribution to mass transport from grain boundary diffusion. Between 3 and 24 h, the hematite has grown in thickness from about 0.5 to about 2 μm . The magnetite has grown from 11–12 to 12 μm and the wustite from 6–7 to about 19 μm .

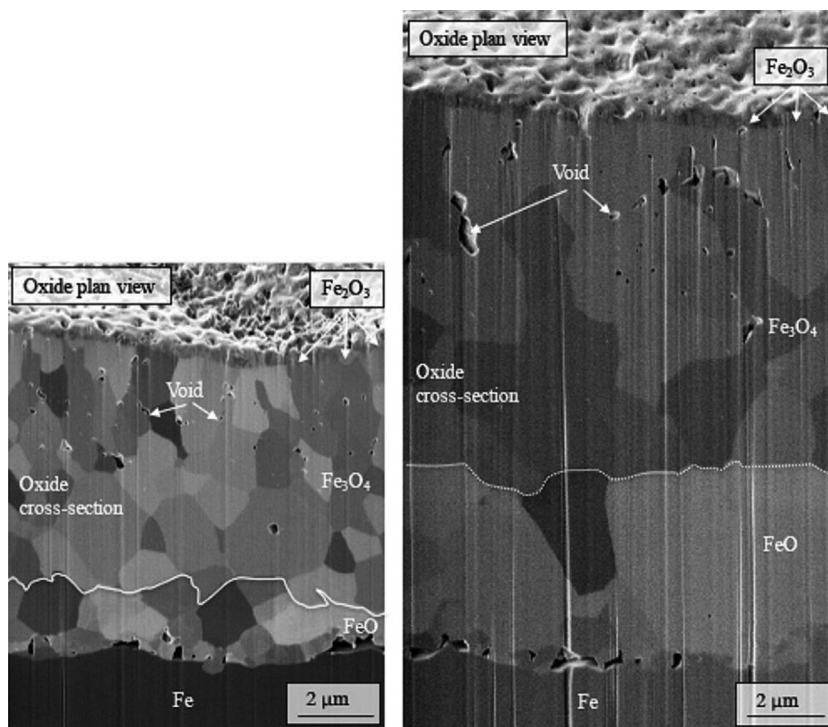


Figure 2. FIB images of cross-sections through the oxide scales formed after 1 and 3 h exposure in dry O_2 at 600 °C. Samples are tilted 45 and 52 degrees.

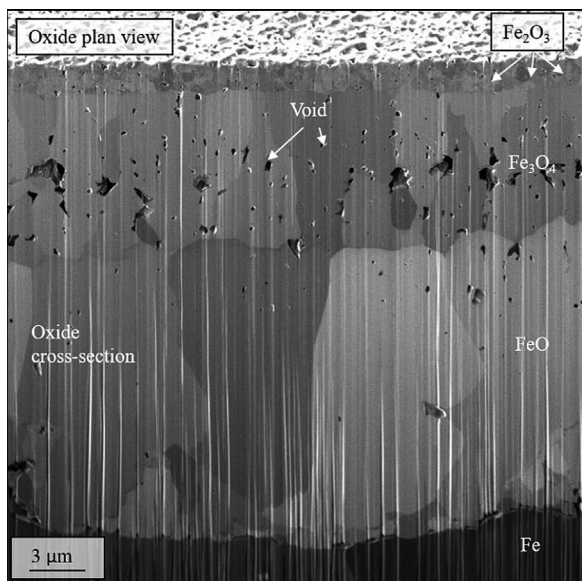


Figure 3. FIB images of cross-sections through the oxide scales formed after 24 h exposure in dry O₂ at 600 °C. The tilt is 52 degrees.

The experimentally measured thicknesses of the oxides as functions of time are shown in Fig. 4 and the overall mass gain as a function of time in Fig. 5.

The formation, and gradual increase of the amount of, presumably, Kirkendall porosity can be observed in Figs. 2 and 3. The amount of Kirkendall porosity has not been quantified, but it clearly forms predominantly in the magnetite. It can also be seen that after 1 and 3 h, the porosity occurs closer to the hematite interface compared to the distribution after 24 h at which time the porosity is more centered in the magnetite layer. Some pores can also be seen at the wustite/ferrite interface.

4.2 Simulation results

Results from simulations are shown in Figs. 6–10. A summary of simulation results and experimental data is presented in Table 1.

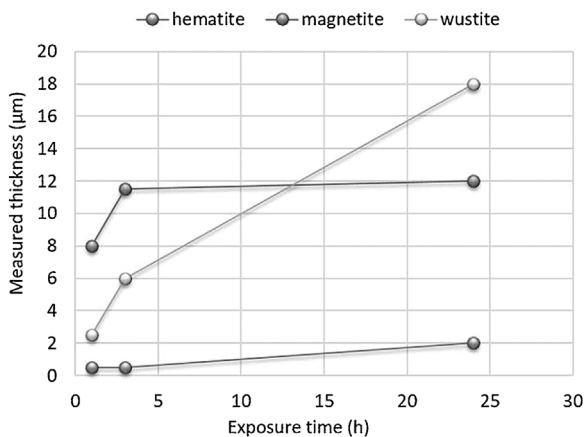


Figure 4. Experimentally measured thickness of the different oxides layers formed after 1, 3, and 24 h exposure in dry O₂ at 600 °C.

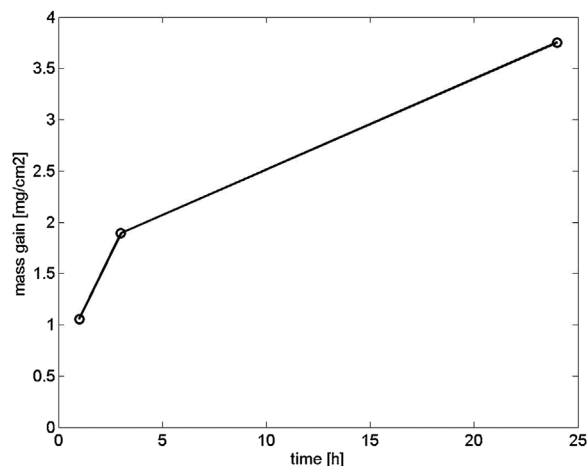


Figure 5. Experimentally measured mass gain [mg/cm²] after 1, 3, and 24 h exposure in dry O₂ at 600 °C.

In this work, the contribution from grain boundary diffusion has only been considered for the magnetite phase. The rationale behind this decision is that the hematite is very thin compared to the other oxides and will only be present in one or two finite volumes (refining the discretization at the surface would drastically increase simulation time) and, further, that the growth of the wustite is not as affected by grain boundary diffusion due to a lower bulk diffusion activation energy. Thus, different values for the factor α was only used for the magnetite phase and in all cases a magnetite grain size of 2 μm was assumed when evaluating the effective mobility. To emphasize this a superscript mag has been added to the factor α used when evaluating the grain boundary contribution.

For numerical reasons it was not possible to have a sufficiently dense grid at the surface to quantitatively resolve the evolution of the thickness of the hematite (The simulations were performed on Linux workstations (Intel Xeon 3.10 GHz 64 GB RAM) and simulation time varied between 27 and 148 h.). Nevertheless, since it is included in the simulation and since it is stable the correct oxygen/iron activities at the hematite/spinel interface are obtained.

Table 1. A comparison between experimental data and results obtained from simulations

Time (h)	Experimental	Simulation results		
		$\alpha^{\text{mag}} = 1$	$\alpha^{\text{mag}} = 0.5$	$\alpha^{\text{mag}} = 0.4$
Total oxide thickness (μm)				
1	11	10	12	16
3	18.5	17	21	28
24	33	50	57	77
Magnetite thickness (μm)				
1	8	1.5	4	10
3	11.5	2	5.5	17
24	12	3.5	14	45
Wustite thickness (μm)				
1	2.5	8.5	8	6
3	6.5	15.5	14.5	11
24	19	46.5	42	32

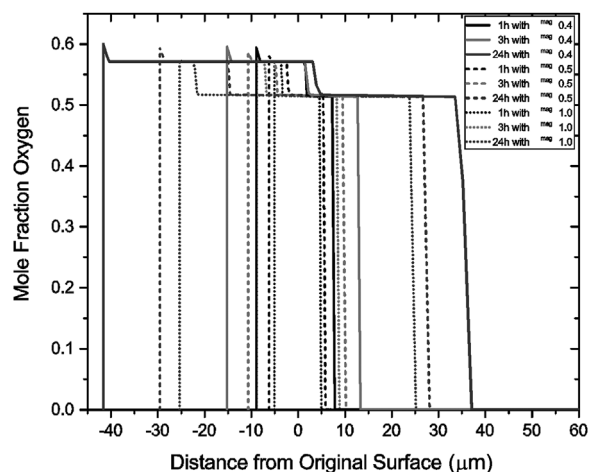


Figure 6. Oxygen profiles obtained for various contributions from grain boundary diffusion. The flux expression used for these simulations is Equation (19).

Oxygen concentration profiles as obtained from simulations are shown in Figs. 6 and 7. Two sets of simulations were performed with different flux equations. Equation (19) was used in the simulations corresponding to Fig. 6 and Equation (21) was used in the simulations corresponding to Fig. 7. It can be seen that the resulting profiles from the two sets of simulations are nearly identical. It should be noted, though, that when Equation (19) was used the mobility of iron in ferrite was set to a value just slightly higher than that in the wüstite for the reason discussed in Section 3.3. When the assessed value for the mobility of iron in ferrite was used in simulations with Equation (19) it was, as qualitatively expected, found that the total oxide thickness was reduced by almost 50% due to the effect of the model to result in a “trans-interface diffusivity” that is rate determining. The suggested modified flux expression, Eq. (21), thus seems to act as intended, in that it removes the effect on the trans-interface diffusivity. However, further investigations in

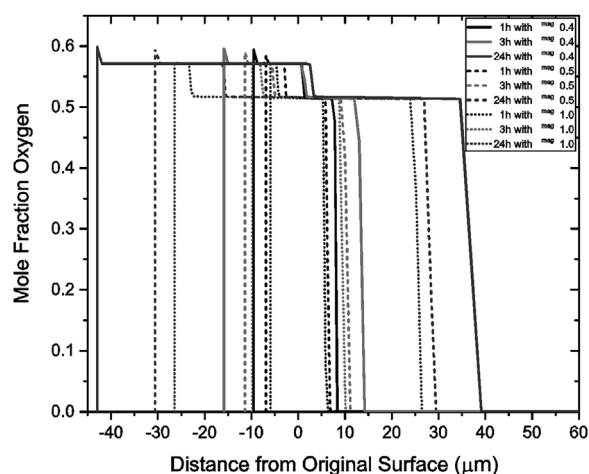


Figure 7. Oxygen profiles obtained for various contributions from grain boundary diffusion. The flux expression used for these simulations is Equation (21).

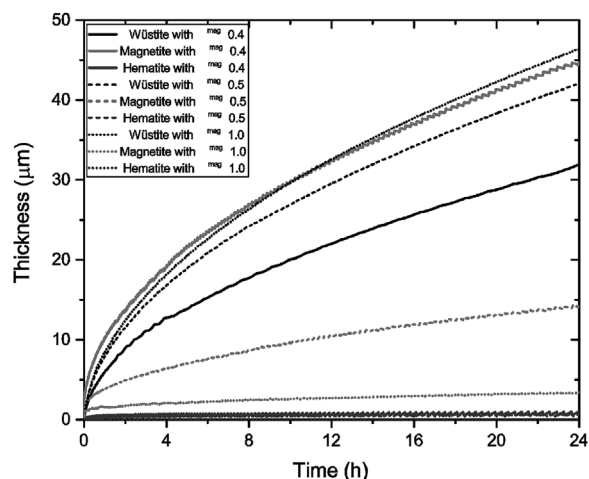


Figure 8. Thicknesses of the individual oxide phases as a function of time calculated for various contributions from grain boundary diffusion. The flux expression used for these simulations is Equation (19).

multicomponent systems are pending. The x-axis variable is the distance from the original surface and it can be seen that the simulation domain grows up to about 40 μm due to the oxygen uptake and the accompanying phase changes. The different phase regions have not been indicated, but the boundaries between them are clearly visible as steps in the oxygen content: The hematite only appears as a thin spike going up to oxygen mole fraction 0.6, then follows the magnetite region, then the wüstite region and finally the ferrite.

The thicknesses of the oxide phases as a function of time are shown in Fig. 8, wüstite as black lines, magnetite as red, and hematite as blue.

Calculated Kirkendall porosity profiles are shown in Fig. 9. As stated above, these profiles can be considered as approximate measures of the maximum amount of porosity that can be expected. In Fig. 10, the Kirkendall porosity profile after 1 h

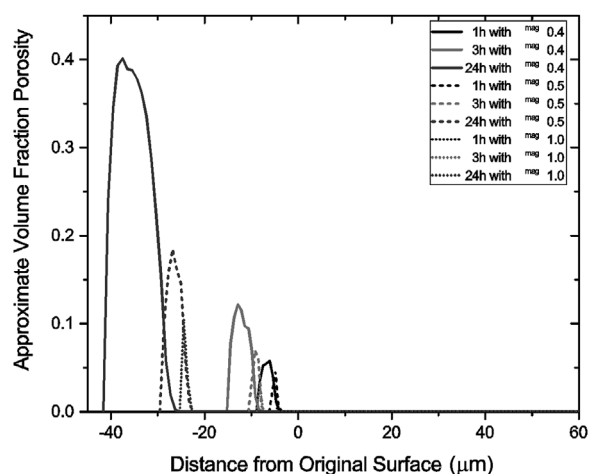


Figure 9. Approximate volume fraction Kirkendall porosity calculated for various contributions from grain boundary diffusion. The flux expression used for these simulations is Equation (19).

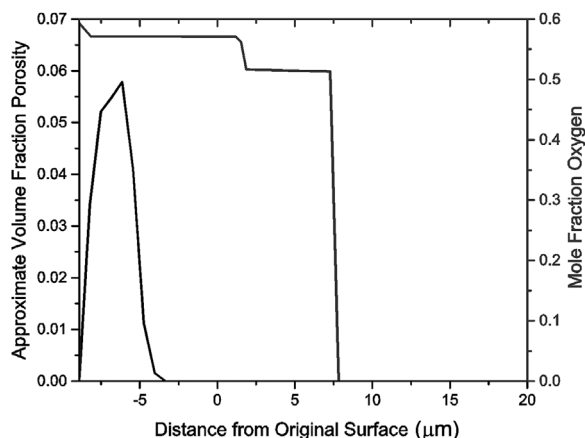


Figure 10. Approximate volume fraction Kirkendall porosity and superimposed oxygen profile after 1 h and assuming $\alpha^{\text{mag}} = 0.4$. The flux expression used for this simulation is Equation (19).

under the assumption $\alpha^{\text{mag}} = 0.4$ is shown along with a superimposed oxygen profile. Figure 10 can be compared with the left hand part of Fig. 2. The agreement between simulation and experiment with regards to the relative position, in the magnetite and toward the surface, and relative amount of the porosity is satisfactory. The agreement with regards to the relative position is less satisfactory after 24 h. After this time, the maximum amount of porosity is still located in the magnetite, but toward the wustite interface. This could be explained by the reasonable assumption that the vacancies are preferably annihilated at existing pores whose relative position has shifted inwards in the specimen as iron has diffused toward the surface.

The total oxide scale thickness obtained from simulations can also be compared to extrapolated experimental data from *Paidassi* [43]. *Paidassi* performed an extensive experimental study of oxidation of iron in air in the temperature range 700–1250 °C. By assuming that the total oxide thickness z^{ox} obeys $z^{\text{ox}} = k^{\text{ox}}(t)^{1/2}$ and fitting an Arrhenius expression $k^{\text{ox}} = k_0^{\text{ox}} \exp(-Q/RT)$ values can be estimated outside the experimental range.

If all of *Paidassi*'s data is included in a least squares fit an activation energy of 85 kJ/mol is obtained and the calculated total oxide scale thickness after 24 h at 600 °C is 62 µm. If only the data up to 800 °C is included an activation energy of 95 kJ/mol and a scale thickness of 51 µm is obtained, though in this case only three data points are used in the evaluation.

5 Discussion

It is important to emphasize that the thermodynamic and kinetic descriptions used in the simulations are independently assessed, i.e., the experimental data that is used for comparison was not used in the assessments. The only adjustable parameter is the parameter α that relates the activation energy for grain boundary diffusion with that for bulk diffusion.

The total oxide thickness obtained in simulations after 24 h is between 50 and 77 µm, depending on the grain boundary contribution, which should be compared with the 33 µm measured experimentally. If, on the other hand, simulation

results are compared with the extrapolated experimental data of *Paidassi*, yielding 51–62 µm, the agreement is satisfactory. According to *Paidassi* the time to reach steady state at 625 °C is 24 h and the time might be significantly longer at 600 °C (see Fig. 12 in Ref. [43]). To clarify this further, experimental exposures of longer duration are needed and this will be the subject of future work.

The variation in the wustite/magnetite thickness ratio with time can at least in part be explained by grain growth and the accompanying changes in the contribution from grain boundary diffusion. In the simulations this ratio varies between 0.7 and 13 after 24 h depending on the choice of α^{mag} . According to *Paidassi* this ratio is about 24 (4/95) in the temperature range 700–1250 °C. Ideally, a separate assessment of the grain boundary diffusivities should be made, similar to the work done by Ref. [44] for Al, Fe, and Ni.

The Calphad approach has been successfully applied in quantitative diffusion process simulations for a number of industrially important material systems, such as steels, superalloys, and aluminum alloys. Diffusion in oxides is inherently much more difficult due to the often very narrow existence intervals of the oxides, the large non-linear kinetic variations, and the importance of grain boundary diffusion. It is nevertheless the authors' hope that the present work has shown the feasibility in applying the Calphad approach also to simulations of oxidation, though much work remain. For example, it may very well turn out that further refinement of the thermodynamic description of one or more oxide phases is necessary. Furthermore, the treatment of grain boundary diffusion may require an altogether new approach. A simulation model similar to the one presented here has already been successfully applied to simulate combined external and internal oxidation of a Ni-base alloy [45]. In that approach diffusion in oxides was not explicitly treated. Instead, the external and internal oxidation was decoupled such that the external oxidation yields a boundary condition on the simulation domain where internal oxidation is simulated.

The model used in the present work is based on the assumption that the material is at all times fully locally equilibrated. This implies that creation and annihilation of defects is not rate controlling. By contrast, *Schwenk and Rahmel* [46] analyzed oxidation of iron and set up rate equations for the interfaces based on reactions involving defects and in their analysis they assumed that the population of each type of defect remain nearly constant. In view of the amount of Kirkendall porosity that is formed during oxidation, it is clear that vacancies are created and annihilated, though this is not proof that an equilibrium amount of vacancies is maintained. The possibility that the concentration and distribution of defects is not at all times equilibrated should be kept in mind in future work.

6 Summary and conclusions

The following specific conclusions can be drawn from this work:

1. A mathematical framework for the modeling of the oxidation of iron is proposed. It allows for the evolution of the important oxidation phases: hematite, magnetite, and wustite.

2. An important attribute of this work is that it makes use of independently assessed thermodynamic and kinetic databases – in other words, the experimental data used to assess the accuracy of the predictions was not used in the assessments.
3. The only truly adjustable parameter is the parameter α which relates grain boundary diffusion to that of bulk diffusion.
4. It has been shown that the variation of the wustite/magnetite thickness ratio can be at least partially explained by grain growth effects and the accompanying changes in contribution from grain boundary diffusion.
5. A powerful feature of the proposed model is its capability for future extension to multicomponent systems, thus involving the diffusion of important elements such as Cr. It has been constructed with that future capability in mind.

Acknowledgements: TJ and HL would like to acknowledge funding from the Swedish Foundation for Strategic Research CROX program and the VINNOVA, Sweden's Innovation Agency, Metallic Materials programme. The authors are grateful to Dr. B. Pujilaksono at the Swedish High Temperature Corrosion center for carrying out the thermobalance experiments. JÅ and HL acknowledges the Hero-m VINN Excellence Center funded by VINNOVA and participating partners.

7 References

- [1] P. Kofstad, *High Temperature Corrosion*, Elsevier Applied Science Publishers, London 1988.
- [2] N. Birks, H. Meier, *Introduction to the High Temperature Oxidation of Metals*, 2nd ed., Cambridge University Press, Cambridge 2006.
- [3] D. Young, *High Temperature Oxidation and Corrosion of Metals*, Elsevier, Amsterdam 2008.
- [4] C. Gleave, J. M. Calvert, D. G. Lees, P. C. Rowlands, *Proc. Royal Soc. A* 1982, 379, 429.
- [5] G. Garnaud, R. A. Rapp, *Oxid. Met.* 1977, 11, 193.
- [6] A. Atkinson, *Rev. Modern Phys.* 1985, 57, 437.
- [7] J. M. Calvert, D. G. Lees, *J. Radioanalytical. Chem.* 1979, 48, 287.
- [8] A. Atkinson, R. I. Taylor, *High Temp. – High Pres.* 1982, 14, 571.
- [9] R. Y. Chen, W. Y. D. Yuen, *Oxid. Met.* 2003, 59, 433.
- [10] O. Kubaschewski, B. E. Hopkins, *Oxidation of Metals and Alloys*, Butterworths, London 1962.
- [11] M. H. Davies, M. T. Simnad, C. E. Birchenall, *Trans. AIME* 1951, 191, 889.
- [12] C. Wagner, *Corros. Sci.* 1969, 9, 91.
- [13] T. Narita, K. Nishida, W. W. Smeltzer, *J. Electrochem. Soc.* 1982, 129, 209.
- [14] S. Hallström, M. Halvarsson, L. Höglund, T. Jonsson, J. Ågren, *Solid State Ionics* 2013, 240, 41.
- [15] J.-O. Andersson, T. Helander, L. Höglund, P.-F. Shi, B. Sundman, *Calphad* 2002, 26, 273.
- [16] H. Larsson, A. Engström, *Acta Mater.* 2006, 54, 2431.
- [17] H. Larsson, L. Höglund, *Calphad* 2009, 33, 495.
- [18] B. Sundman, *J. Phase Equilibria* 1991, 12, 127.
- [19] T. Hidayat, D. Shishin, E. Jak, S. A. Deckerov, *Calphad* 2015, 48, 131.
- [20] M. Hillert, *J. Alloys Compd.* 2001, 320, 161.
- [21] O. Redlich, A. T. Kister, *Ind. Eng. Chem.* 1948, 40, 345.
- [22] G. Inden, *Zeitschrift Fuer Met. Res. Adv. Tech.* 1975, 66, 577.
- [23] M. Hillert, M. Jarl, *Calphad* 1978, 2, 227.
- [24] L. Kjellqvist, M. Selleby, B. Sundman, *Calphad* 2008, 32, 577.
- [25] R. Naraghi, in manuscript.
- [26] S. Hallström, L. Höglund, J. Ågren, *Acta Mater.* 2011, 59, 53.
- [27] S. Hallström, *PhD Thesis*, Department of Materials Science and Engineering, KTH, Stockholm 2014.
- [28] J. Takada, S. Yamamoto, S. Kikuchi, M. Adachi, *Metall. Trans. A* 1986, 17A, 221.
- [29] B. Jönsson, *Z. Metallkde.* 1992, 83, 349.
- [30] I. Kaur, W. Gust, *Fundamentals of Grain and Interphase Boundary Diffusion*, 2nd ed., Ziegler Press, Stuttgart 1989.
- [31] J. Bardeen, *Phys. Rev.* 1949, 76, 1403.
- [32] H. Strandlund, H. Larsson, *Metall. Mater. Trans. A* 2006, 37A, 1785.
- [33] O. Wiener, *Abh. Mat.-Phy. Kön. Sächs. Ges. Wis.* 1912, 32, 509.
- [34] Z. Hashin, S. Shtrikman, *J. Appl. Phys.* 1962, 33, 3125.
- [35] M. Hillert, *Scripta Mater.* 2001, 44, 1095.
- [36] H. Larsson, H. Strandlund, M. Hillert, *Acta Mater.* 2006, 54, 945.
- [37] H. Larsson, A. Borgenstam, *Scripta Mater.* 2007, 56, 61.
- [38] N. Matan, H. M. A. Winand, P. Carter, M. Carutaratne, P. D. Bogdanoff, R. C. Reed, *Acta Mater.* 1998, 46, 4587.
- [39] L. Höglund, J. Ågren, *Acta Mater.* 2001, 49, 1311.
- [40] H. Strandlund, H. Larsson, *Acta Mater.* 2004, 52, 4695.
- [41] T. Jonsson, B. Pujilaksono, A. Fuchs, J.-E. Svensson, L.-G. Johansson, M. Halvarsson, *Mater. Sci. Forum* 2008, 595–598, 1005.
- [42] B. Pujilaksono, T. Jonsson, M. Halvarsson, J.-E. Svensson, L.-G. Johansson, *Corros. Sci.* 2010, 52, 1560.
- [43] J. Paidassi, *Acta Metall.* 1958, 6, 184.
- [44] G. Stechnauer, E. Kozeschnik, *Calphad* 2014, 47, 92.
- [45] A. Chyrkin, W. G. Sloof, R. Pillai, T. Galiullin, D. Gruner, L. Singheiser, W. J. Quadackers, *Mater. High Temp.* 2015, 32, 102.
- [46] W. Schwenk, A. Rahmel, *Oxid. Met.* 1986, 25, 293.

(Received: November 30, 2015)

W8781

(Accepted: March 18, 2016)